Journal of Zhejiang University-SCIENCE A (Applied Physics & Engineering)
ISSN 1673-565X (Print); ISSN 1862-1775 (Online)
www.jzus.zju.edu.cn; www.springerlink.com
E-mail: jzus@zju.edu.cn

Design and numerical simulation of a clamshell-shaped inlet cover for air-breathing hypersonic vehicles*

Xun WEN†, Jun LIU, Jie LI, Feng DING, Zhi-xun XIA†‡
College of Aerospace Science and Engineering, National University of Defense Technology, Changsha 410073, China
†E-mail: xwentst@163.com; xiazhixun@sina.com

Received Nov. 2, 2018; Revision accepted Mar. 27, 2019; Crosschecked Apr. 3, 2019

Abstract: An efficient clamshell-shaped inlet cover configuration based on a shockwave interference methodology is proposed, which has the advantage of an autonomous opening using the aerodynamic force and moment. A preliminary design method for the inlet cover is introduced and used to produce cover models of two different lengths, with contributions similar to those of cowlings, rocket fairings, shrouds, or false ogives. The clamshell-shaped inlet cover features a practical design with a wide range of applications, including utilization in air-breathing hypersonic vehicles under specific constraints. In this investigation, aerodynamic numerical simulations were conducted to evaluate the extent to which the objectives and design principles are achieved for two typical ballistic separation states. The results show that both configurations can prevent an excessive accumulation of shockwaves in the nose cone area. In addition, the inlet cover generates negative lift, which results in the generation of an opening moment. The calculated heat flux at the leading edge of the clamshell-shaped inlet cover is approximately 13 MW/m^2, which is within the limit of the composite material but slightly higher than that of the stagnation point of the nose cone.

Key words: Aerodynamic configuration design; Novel inlet cover; Aerodynamic force; Heat evaluation
https://doi.org/10.1631/jzus.A1800620 **CLC number:** V43

1 Introduction

The production of air-breathing hypersonic vehicles has attracted significant interest in recent decades (Lockwood et al., 1999; McClinton et al., 2005; Sziroczak and Smith, 2016; Lv et al., 2017; Liao et al., 2018). In particular, the design of their inlet covers or shrouds has attracted significant attention because it is well known that the configuration of such components can greatly reduce the shockwave oscillation in the blind cavity of the engine during the boost phase. For the launching of rocket payloads, conventional payload fairings are typically designed with a curved surface for rotation (Morshed et al., 2013; Kosareo et al., 2014); however, these fairings are inappropriate for air-breathing hypersonic vehicles because they require heavy and potentially hazardous explosive bolts. In this investigation, a tectonic line method for producing an inlet cover suitable for a wide range of inlet scales is proposed. The configuration has significant economic potential and a wide range of possible applications with no risk of an explosion because it can open automatically using aerodynamic forces.

To date, many researchers have investigated fairing designs and optimization using numerical simulations and experiments. Yang et al. (2014) employed the Kriging approximation method to establish a library of aerodynamic parameterized fairing models and identified the optimal parameters for decreasing the average drag by 22.2% compared with

---

‡ Corresponding author

* Project supported by the National Natural Science Foundation of China (Nos. 11702322 and 11572348) and the Joint Funds of the National Natural Science Foundation of China (No. U1730247)

ORCID: Xun WEN, https://orcid.org/0000-0002-7629-5576

the benchmark, where the alternative constraints satisfied the design requirements. Zhao et al. (2017) used a large eddy simulation method to evaluate the fairing configurations with different scales, including a conventional ball-cone shape, power-rate curve profile, and von Karman curve shape. Higgins et al. (2008) investigated the fairing system for the Minotaur IV launch vehicle in collaboration with the US Air Force Research Laboratory. The synchronized forces, strain, and displacement were investigated and compared with pretest predictions. In addition to a conventional spin configuration, there are several other specially shaped fairing design approaches (Colonno and Alonso, 2008; Blades and Newman III, 2013; Groves et al., 2014). However, most of the design methods in previously published reports have targeted the payload fairing; there are few fairing configurations suitable for air-breathing hypersonic vehicles, particularly those with submandibular inlets. Without a payload, the large unoccupied spaces in payload fairings are burdensome and wasteful for hypersonic vehicle applications and can be considered an unnecessary design surplus.

Furthermore, the reliability of the inlet cover system is determined mainly through a validation of the material separation, which is conducted using a numerical simulation method that includes a qualitative judgment under a steady state and a trajectory judgment under an unsteady state (Murman and Diosady, 2016). For a submandibular inlet cover designed as part of an investigation (Wang et al., 2016), a separation experiment was conducted in a wind tunnel under Mach 6.0 conditions for verification. The experimental separation track was compared with the numerical results without considering the thermal effects on the aircraft, and the thermal protection under the cone was not discussed. Brauckmann et al. (2015) analyzed the effects of different nose shapes, including a spherically blunted on-axis cone as the baseline, a canted version of the baseline nose, a blunt on-axis version, a canted version of the blunt nose, an on-axis ogive shape, and a canted ogive shape, on the aerodynamic characteristics of the boosters. A series of experiments were also conducted to examine the problem of inlet plugging, including an unsteady inlet opening process (Zhang et al., 2017). In this investigation, an innovative design concept was adopted to create a practical self-separating inlet cover configuration, which was verified through the numerical results in terms of both aerodynamic forces and heat.

With the rapid development of hypersonic vehicles, conventional large-scale rotary fairings cannot satisfy the requirements for various indicators in the field. A new type of flexible, practical inlet cover configuration is therefore urgently needed. The tectonic line design method and proposed configuration presented in this paper aim to address the problem of a redundant payload space while simultaneously reducing the weight of the fairing system. A numerical analysis was conducted by taking into account the flow field, and the design concept for the inlet covers was elucidated. The proposed configuration is reliable in principle and is simple to construct. The simulation results provide general guidance regarding aerospace product diversification.

2 Design principle of inlet cover

In hypersonic vehicles, the precursor shockwave may interact with the bow shockwave at the leading edge of the wings, lips, or inlets. Shockwaves or shock interactions complicate the flow field near the shear layer and generate various flow structures. To avoid strong reflections of the shockwaves onto the fragile cone made of a wave-transmitting material (Fig. 1), it is necessary to design the shape of the front edge of the inlet cover appropriately. The inlet cover used for the new design concept proposed in this study was generated using curve lofting on the base plane.

As shown in Fig. 2, the inlet cover consists of a front separation surface identified as “1”, a transition surface identified as “2”, and a lower surface identified as “3”, in addition to the rear surface consisting of a baffle in the tail. For a convenient setting of the parameters used in this configuration, the von Karman cone was selected as the head nose of the vehicle. The inlet cover design concept and generation methods are based on the following equations:

$$\theta=\arccos\left(1-\frac{2x}{L}\right), \tag{1}$$

$$y=\frac{R}{\sqrt{\pi}}\sqrt{\theta-\frac{\sin(2\theta)}{2}+C\sin^3\theta}, \tag{2}$$

$$\begin{cases} R_1 = y(x_1, \varphi), \\ R_2 = R_1 + H, \end{cases} \tag{3}$$

where θ is the Karman curve angle, x is X direction coordinate, y is Y direction coordinate, L is the length, R is the radius of head nose, C is the Karman curve constant, R_1 and R_2 are the radii of upper edge and lower edge for the inlet cover, respectively, x_1 is the X direction location of the inlet, φ is the geometry angle, and H is the height of inlet cover. Eqs. (1)–(3) represent the functions of the von Karman cone and baffle at the trailing edge of the base plane, as indicated in Fig. 3.

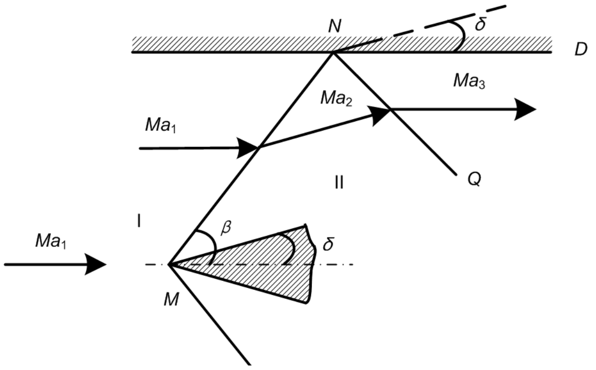

Fig. 1 Flow through the nose cone

Ma_1: coming Mach number; Ma_2: Mach number after the first reflection; Ma_3: Mach number after the second reflection; β: shock wave angle; δ: wedge angle

Fig. 4 shows the locations of the design points of the configuration on the flow plane. To achieve a desirable and exclusive flow field at the original entrance to the inlet for a state of separation, the front of the inlet cover on the longitudinal symmetry plane was designed to be a cubic B-spline curve. At the exterior margin of the inlet cover on the base plane, curves $P_1P_2P_1'$ and $P_6P_5P_6'$ in Fig. 4 were both designed to be secondary B-spline curves of polynomial functions to improve the smoothness of the transition.

Depending on the separation Mach number and incoming flow, the head nose of the vehicle generates a shockwave line, which is symbolically represented as the dashed line OP_5' in Fig. 5. Point P_5 should be located on line OP_5' or outside the area XOP_5'. To determine appropriate ranges of the length and height of the inlet, unique ideal locations for points P_5 and P_6'' can be initially identified, where curve P_5P_6'' is a horizontal curve. Subsequently, an angle $P_4P_5P_5''$ is selected that is smaller than that between the ray P_2P_3

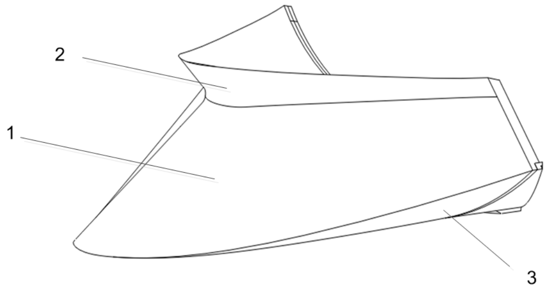

Fig. 2 Illustration of the novel inlet cover

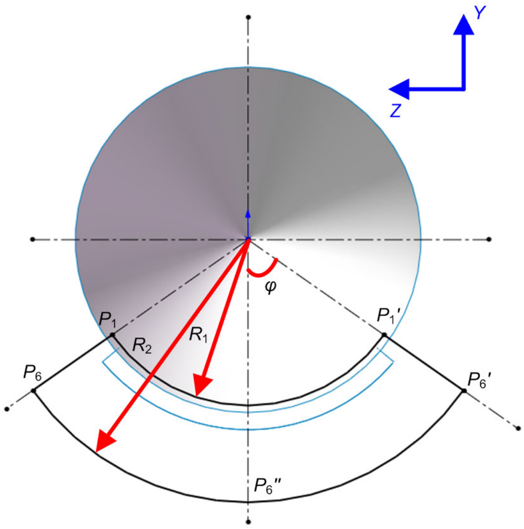

Fig. 3 Preliminary sketch of baffle in the tail

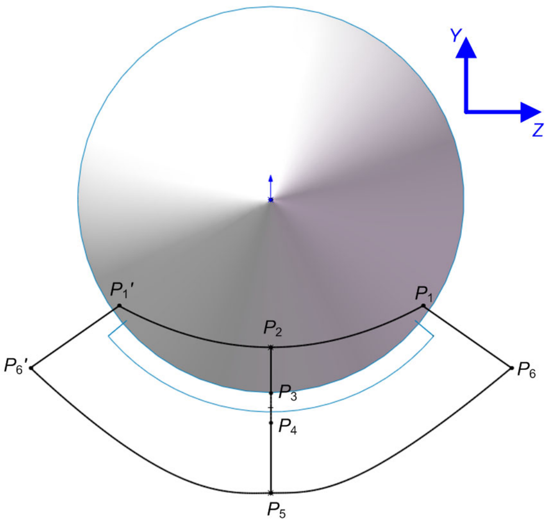

Fig. 4 Front view of locations of key points

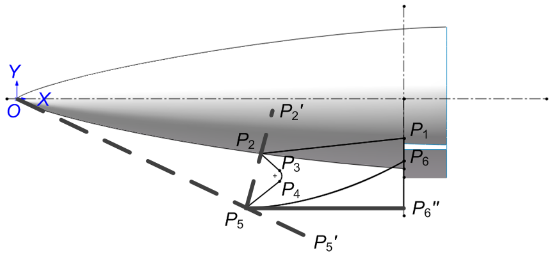

Fig. 5 Schematic illustration of tectonic line method

and X direction and satisfies the condition in which the center of the arc trajectory of P_3P_4 is higher than the inlet cover shaft on the base plane. Consequently, point P_2 will then be located on the vehicle's surface within the dashed line P_5P_2', which is the theoretical shockwave line generated by the wedge separation surface. Therefore, the ultimate external design parameters of the inlet cover can be confirmed from the relevant points and curves; the specific curve functions and design parameters are shown in Section 3.

3 Physical models and numerical conditions

3.1 Physical models

By using the tectonic line design method, a physical model of the hypersonic vehicle forebody was generated based on the separation state, which consists of an inlet cover and vehicle head nose. The clamshell-shaped inlet cover has three key surfaces, which are identified in Fig. 6b as the front, lower, and rear surfaces. Each of these surfaces serves an aerodynamic purpose. As shown in Fig. 2, the front surface consists of two parts. The main part has a normal vector that points upward and mainly provides the separation force at the stage transition. The other part has a downward-pointing normal vector, and transitions between and connects the head and inlet cover. Based on the components of the separation and transition surfaces, the front surface will contribute to the main separation force and prevent the shockwave from hitting the nose cone. Without the rear or lower surface, there will inevitably be a cavity at the end of the configuration, and the air inlet of the vehicle will not be shielded or closed over. Thus, the rear surface will serve to deflect the backflow, and the lower surface will ensure the integrity of the entire profile.

The two inlet covers analyzed in this study were designed using the parameters listed in Table 1. The different inlet positions result in the final length discrepancy of the inlet cover, together with the line-type of the leading edge described in Eqs. (4)–(6):

$$x_{\mathrm{I}}=\begin{cases}A_{11}y+B_{11}, & y\in(Y_{P_3},Y_{P_2}),\\ A_{12}y+B_{12}, & y\in(Y_{P_5},Y_{P_4}),\end{cases}\tag{4}$$

$$x_{\mathrm{II}}=\begin{cases}A_{21}y+B_{21}, & y\in(Y_{P_3},Y_{P_2}),\\ A_{22}y+B_{22}, & y\in(Y_{P_5},Y_{P_4}),\end{cases}\tag{5}$$

$$\boldsymbol{A}=\begin{bmatrix}-1.026 & 348\\ 1.500 & 920\end{bmatrix},\ \boldsymbol{B}=\begin{bmatrix}-1.083 & 644\\ 1.278 & 1286\end{bmatrix},\tag{6}$$

where x_{I} and x_{II} are equations of design parameters for profiles I and II, respectively.

Table 1 Design parameters of the inlet cover

Design parameter	Value
Mach number, *Ma*	6.5
Attack angle, α (°)	0
Length, L (mm)	1500
Radius of head nose, R (mm)	250
Karman curve constant, C	0
Height of inlet cover, H (mm)	140
Inlet location in X direction, x_1 (mm)	1350
Geometry angle, φ (°)	55

Table 2 lists the mass properties of clamshell-shaped inlet covers made of a high-temperature composite material. Fig. 6 presents the 3D illustrations of the inlet covers.

3.2 Numerical approach

The aerodynamic characteristics of the inlet cover have important effects on the aircraft control and structural design, particularly the lift and drag characteristics. Owing to the wide range of speeds encountered by the operational envelope, the final design must satisfy several, often contradictory, requirements. However, the main focus is a reduction of drag during the ascent phase and inlet cover separation before cruising. Considering *Ma*=6.5 below a height of 26 km and *Ma*=6.5 below a height of 19 km, which correspond to the principle verification of the aerodynamic separation design and the worst condition during flight, respectively, two typical ballistic states were selected as assessment standards to evaluate the ability of the proposed shape design to achieve the required aerodynamic separation goals. The relevant specific state parameters of the inlet cover separation point and the moment of booster separation are shown in Table 3.

The implicitly coupled Reynolds-averaged Navier–Stokes equation and shear-stress-transport turbulence model were employed to calculate the flow fields and aerodynamic performance using the commercial software ANSYS Fluent. Spatial discretization is a cell-based finite-volume-type method with first-order upwind values, and the time is discretized using the Runge–Kutta method. For the incoming flow state parameters, the initial boundary condition applied by Ding et al. (2015) and Liu et al. (2017) was adopted. A computational fluid dynamics analysis was conducted under the assumption of laminar flow conditions for the heat flux. The surface heat flux was calculated using the concept of enthalpy, and the stagnation heat flux was measured through the model scale. The values of the other parameters were determined based on the thickness of the new boundary layer and new edge points of the boundary layer applied by Li et al. (2016).

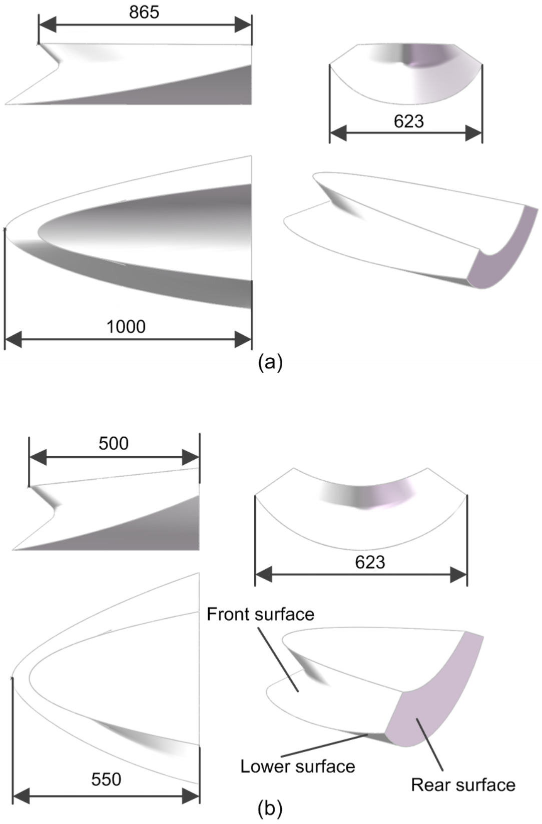

Fig. 6 Three views of each inlet cover (unit: mm)
(a) Profile I; (b) Profile II

4 Results and discussion

4.1 Verification of inlet cover design

The aerodynamic performance of hypersonic vehicles is an area of great concern. Table 4 lists the aerodynamic characteristics of the inlet covers under a state of fairing trajectory separation. The configurations are well adapted to both the lip position and length, and produce a negative lift. The shaft vector direction ranges from point position (1500, −255, 30) to (1500, −255, −30) (mm). Thus, the positive value of the moment indicates a closing trend, as illustrated in Fig. 7. The initial moment is 1998 N·m for profile I and 1488 N·m for profile II, as shown in Table 4. These values are consistent with the original design objective for the front surface, as shown by the schematic diagram in Fig. 8. The analysis of the force

Table 2 Quality characteristics

Shape No.	Mass (kg)	Centroid position (mm)	Shaft coordinate (mm)
Profile I	50	(964, −269, 0)	(1500, −255, 30)→(1500, −255, −30)
Profile II	25	(1163, −269, 0)	(1500, −255, 30)→(1500, −255, −30)

Table 3 Ballistic characteristics of states

Characteristic state	*Ma*	Height (km)	Dynamic pressure, D_p (kPa)	Tempreture, *T* (K)	Pressure, *p* (Pa)	*α* (°)
Fairing separation point	6.5	26	64	222	2153	0
Booster separation point	6.5	19	189	217	6410	0

Table 4 Force and moment in clamshell inlet cover separation state

Component	Profile I of inlet cover			Profile II of inlet cover		
	M_p (N·m)	F_D (N)	F_L (N)	M_p (N·m)	F_D (N)	F_L (N)
Front surface	−1979	3521	−2621	−1536	5687	−3121
Lower surface	−16	0	−100	51	0	90
Rear surface	−3	171	0	−3	164	0
Entire cover	−1998	3692	−2721	−1488	5851	−3031

M_p: moment of force for opening inlet covers; F_D: aerodynamic drag; F_L: aerodynamic lift

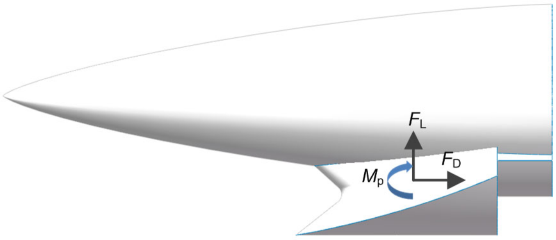

Fig. 7 Illustration of positive lift and closing tendency

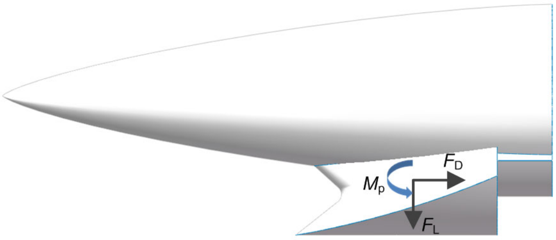

Fig. 8 Illustration of negative lift and opening tendency

components indicates that the front line contributes to the opening and separation. This has not been previously achieved and was the impetus for designing and selecting this configuration. In addition to a negative lift, the configuration generates a drag of approximately 3.5 kN for profile I and 5.7 kN for profile II, which are typical values for contemporary booster rockets.

The typical pressures on the surface upon booster separation are given in Table 5, which suggest that the inlet cover has less influence on the force in the main area of the nose cone. To a certain extent, this configuration can satisfy the shockwave interference control requirement for the head cone area of influence. In addition, curve $P_2P_3P_4P_5$ strongly affects the peak value at the front edge of the fairing; hence, the line type should be carefully designed for the inlet lip configuration of a specific aircraft.

Table 5 Analysis of peak pressure and most of the area of the nose cone

Component	$\overline{P}_{\max}$	$P_{\max}$ (Pa)	$\overline{P}_{A}$	P_A (Pa)
Profile I	140	386 960	10	27 640
Profile II	123	254 289	10	27 640

$\overline{P}_{\max}$: dimensionless pressure peak; $P_{\max}$: pressure peak; $\overline{P}_{A}$: dimensionless pressure at mostly area on the head nose; P_A: pressure at mostly area on the head nose

The moment of booster separation, which represents the worst and most risky flight state, was analyzed, and the flow field on the longitudinal symmetric plane was obtained, as shown in Fig. 9. Fig. 9a shows that the incoming flow produces a bow shock at the cone and then flows through the lower surface of the cone and stops before the separation surface of inlet cover I. However, the flow field structure near the inlet cover has more complex characteristics. Shockwaves from different wedge surfaces of the inlet cover intersect at the inlet cover waist, generating a high-pressure zone formed by three high-pressure points. This indicates that oblique shockwaves are generated separately to form a high-pressure zone near the inlet cover waist, which contributes to the separation. As shown in Fig. 9b, the area affected by the shockwave interference decreases; in addition, the length of the inlet cover is shortened, and the bow shockwave fails to arrive at cover II, resulting in a more reasonable and acceptable flow field structure. The analysis presented above validates the design methodology in which two leading-edge configurations of the inlet cover play an important role in protecting the wave-transmitting material by controlling the shockwave strain.

Figs. 10 and 11 present the individual surface dimensionless pressure distribution contours. As viewed from the front in Fig. 10a, a high-pressure area appears in the middle, and two high-pressure

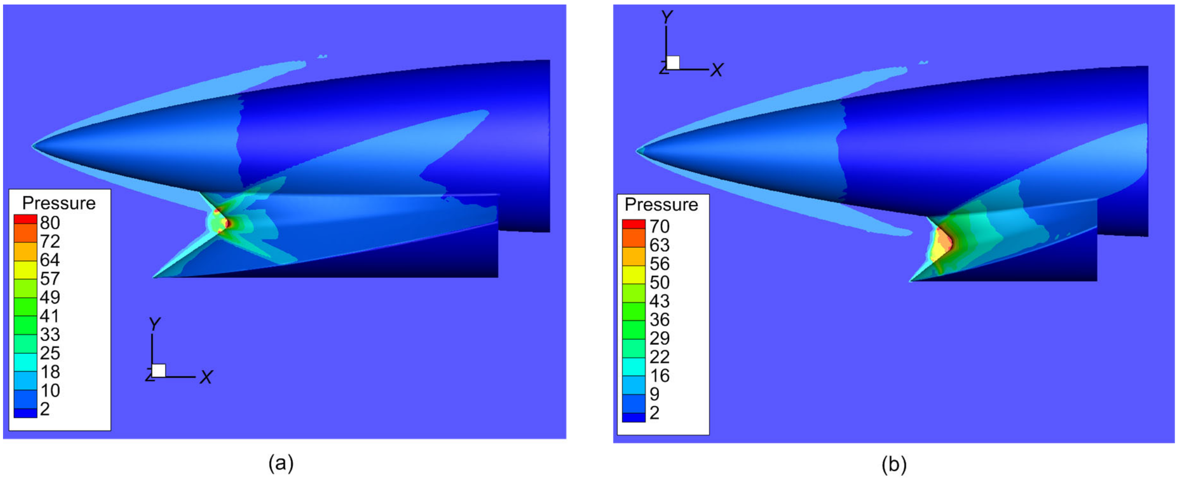

Fig. 9 Dimensionless pressure contours on the longitudinal symmetric plane
(a) Profile I; (b) Profile II

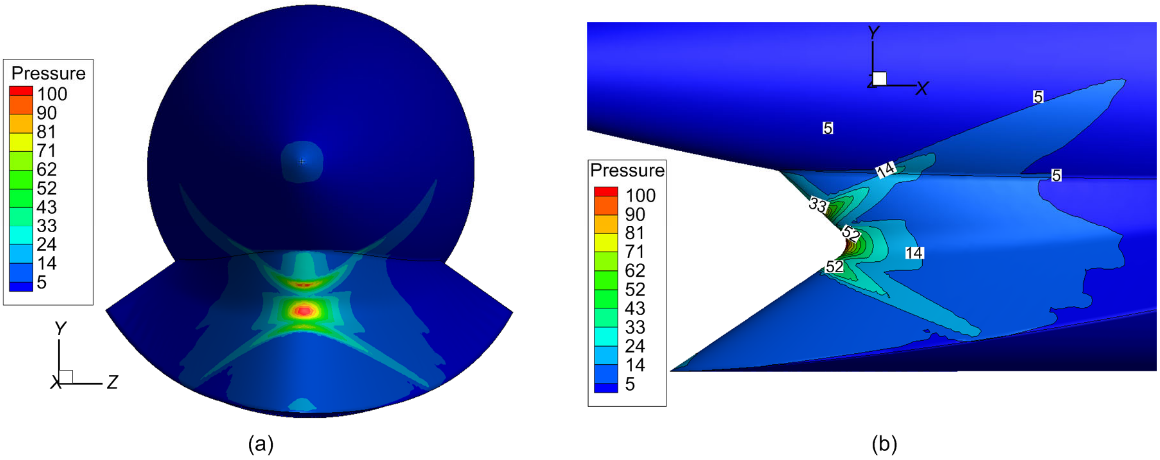

Fig. 10 Surface dimensionless pressure distribution contours of Profile I
(a) Front view; (b) Side view

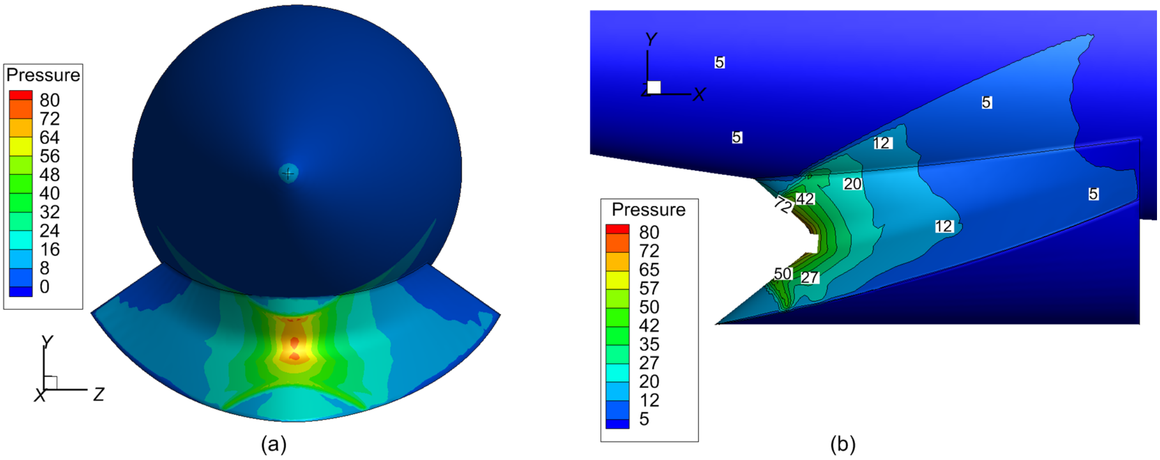

Fig. 11 Surface dimensionless pressure distribution contours of Profile II
(a) Front view; (b) Side view

points are located nearby. The surface pressure forms an X-shaped symmetrical distribution pattern, which interferes slightly with the surface underneath the head cone. As shown in Fig. 10b, the high-pressure points are distributed mainly near the fairing's leading edge and prevent shockwaves from hitting the compression surface of the cone. The head-cone pressure distribution is acceptable, owing to the pressure of the boundary layer. Compared with that of profile I, the surface pressure of profile II in Fig. 11a is distributed more uniformly, without an obvious X-shaped pattern. The side view of profile II in Fig. 11b shows a section of the fan with pressure fluctuations, which is different from profile I. Similarly, the side view of profile I in Fig. 10b shows pressure fluctuations in three directions, which generally spread along the flow such that the maximum fluctuation occurs in the central area, which has the fastest attenuation. However, the minimum fluctuation occurs in the lower area, which has the greatest spread. As shown in the side views in Figs. 10b and 11b, we found that the distribution of the force of profile II is more uniform than that of profile I. A more uniform distribution of the force results in a better heat transfer and less shear stress. In the front views in Figs. 10a and 11a, the dimensionless peak pressure in profile I is approximately 100, and that in profile II is approximately 80. Therefore, it can be concluded that profile II performs better against aerodynamic forces than profile I owing to the low peak pressure and uniform distribution of the force.

4.2 Aerodynamic thermal analysis

Similarly, because the booster separation state is the riskiest and threatens the state of the flight trajectory, the thermal aerodynamic behavior is investigated, and preliminary numerical analysis results are presented in this section. The front views of the surface heat flux in Figs. 12 and 13 show that the heat flux (Q_t) distributions of the two fairings have the same shape, but the quantitative values differ. The heat flux distribution acts in concert with the pressure distribution, such that the configuration generates oblique shockwaves at the lower and wedge surfaces; a shockwave intersection appears only at the front of the inlet cover, although it is distinct. A larger contour gradient implies stronger converging shockwaves. In the side views in Figs. 14 and 15, the contours are densely concentrated, mainly on the front surface of the inlet cover and somewhat on the lower surface of the head. In addition, a heat flux stagnation zone

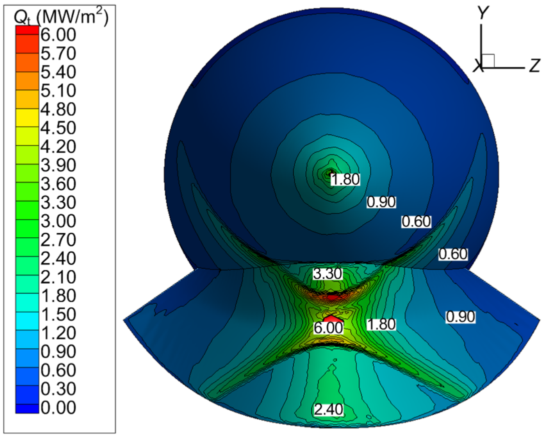

Fig. 12 Front heat flux distribution on profile I

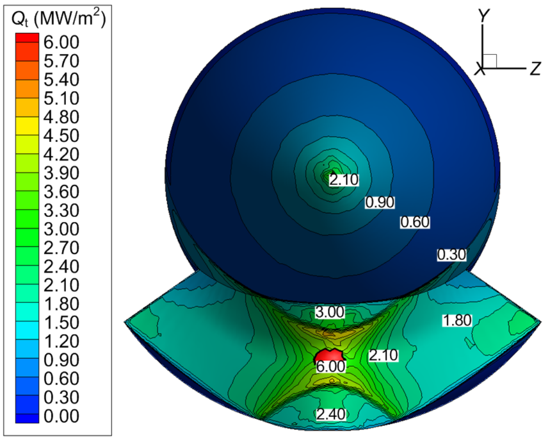

Fig. 13 Front heat flux distribution on profile II

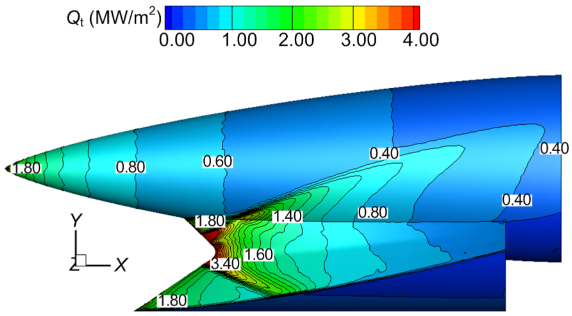

Fig. 14 Side heat flux distribution on profile I

appears at the edge, where the worst thermal environment is encountered. Although high heat occurs near the leading edge of the inlet cover, an anomalous heat flux point cannot be seen at the front of the cone. Figs. 14 and 15 show that the heat flux is approximately 1.2 MW/m^2 in the main area of the cone, which consists of a brittle wave-transmitting material; this value compares well with the conformity constraints.

Figs. 16–19 show the heat flux values on the upper and lower surfaces of the profiles. The curves indicate that the heat flux at the cone tip is approximately 11.2 MW/m^2; the heat flux of the front component of the inlet cover is approximately 13.5 MW/m^2 for profile I and 12.5 MW/m^2 for profile II, and the heat flux from most of the other areas is less than 5.0 MW/m^2. These values are within the limits of the material used in the design, which is the most popular ceramic nanomaterial with a laminated structure on the market. This lightweight thermal protection material, 30 mm in thickness, can tolerate extremely high temperature environments of up to 1700 °C (Hong et al., 2013). It was also determined that the peak heat flux that occurs at the leading edge of profile II is slightly lower than that of profile I because the greater distance from the leading edge to the head shockwave has less effect on the heat. Nevertheless, the heat fluxes of the upper meridian of the profiles are in good agreement.

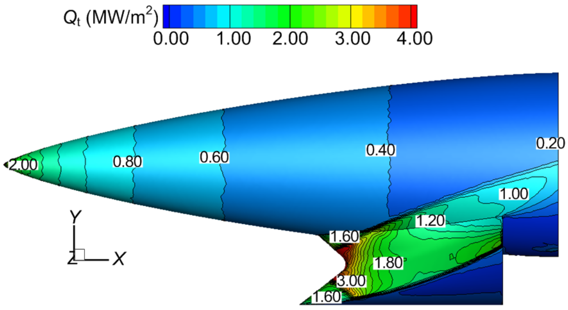

Fig. 15 Side heat flux distribution on profile II

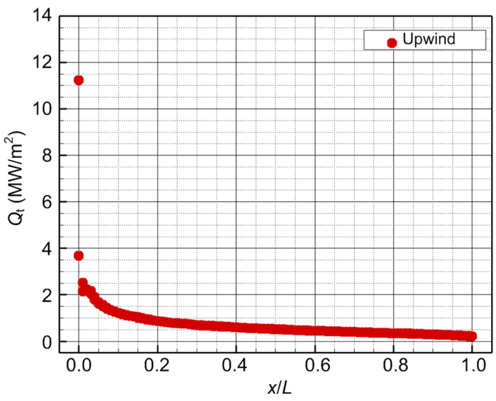

Fig. 16 Heat flux in upper meridian for profile I

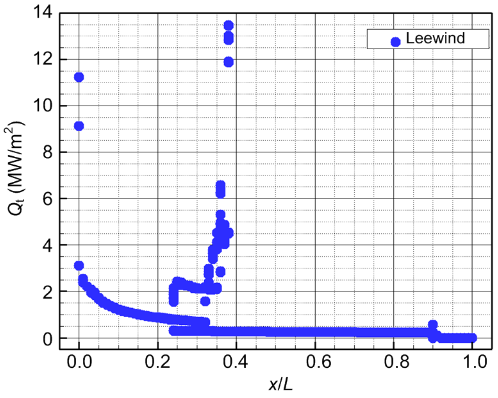

Fig. 17 Heat flux in lower meridian for profile I

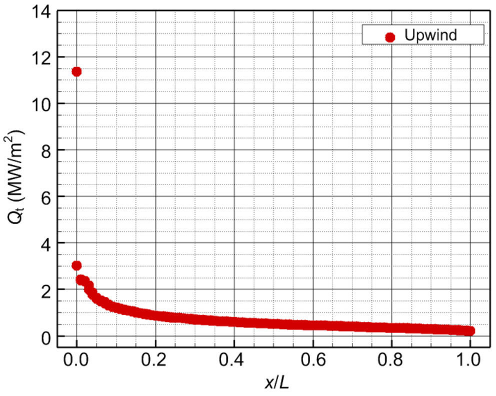

Fig. 18 Heat flux in upper meridian for profile II

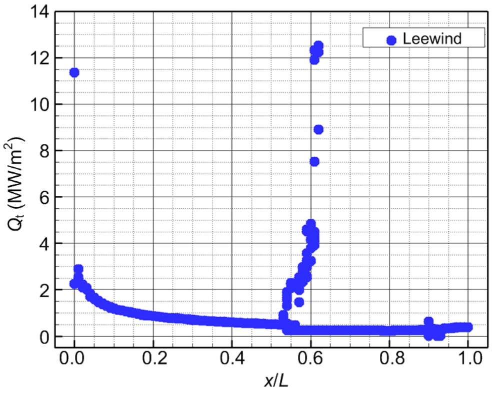

Fig. 19 Heat flux in lower meridian for profile II

5 Conclusions

Using the theory of shockwaves and shockwave interactions, a design method for an aerodynamic self-separating clamshell-shaped inlet cover was proposed. An aerodynamic shape of the inlet cover was designed, and the cover was modeled as a forebody for air-breathing hypersonic vehicles. Two generated profiles, which corresponded to two different lip configuration lengths, were investigated numerically. The convenient commercial flow solver was employed to evaluate the force and heat on the inlet cover surface. The numerical results showed that there was no obvious high-pressure zone or high-heat zone on the nose cone area during installation of the cover model, which indicates that the shockwave distribution was well controlled. Moreover, the inlet cover can produce a negative lift, with a tendency toward an automatic opening. The cover conforms to the design principles of shockwave interference and facilitates an automatic opening and separation, simplifying the mechanical structure. These results were consistent with the original intent of the design and were verified through numerical simulations. Finally, the heat flux peak was also evaluated to provide general guidance on future project engineering processes; in addition, the heat flux of the inlet cover's front component was approximately 13.5 MW/m^2 for profile I and 12.5 MW/m^2 for profile II.

References

Blades EL, Newman III JC, 2013. Computational-fluid-dynamics-based design optimization of a large asymmetric payload fairing. *Journal of Spacecraft and Rockets*, 50(5):1013-1023. https://doi.org/10.2514/1.A32301

Brauckmann GJ, Streett C, Kleb WL, et al., 2015. Computational and experimental unsteady pressures for alternate SLS booster nose shapes. Proceedings of the 53rd AIAA Aerospace Sciences Meeting. https://doi.org/10.2514/6.2015-0559

Colonno MR, Alonso JJ, 2008. The optimum launch vehicle fairing: an MDO approach. Proceedings of the 12th AIAA/ISSMO Multidisciplinary Analysis and Optimization Conference. https://doi.org/10.2514/6.2008-5883

Ding F, Shen CB, Liu J, et al., 2015. Influence of surface pressure distribution of basic flow field on shape and performance of waverider. *Acta Astronautica*, 108:62-78. https://doi.org/10.1016/j.actaastro.2014.11.038

Groves CE, Ilie M, Schallhorn PA, 2014. Computational fluid dynamics uncertainty analysis for payload fairing spacecraft environmental control systems. Proceedings of the 52nd Aerospace Sciences Meeting. https://doi.org/10.2514/6.2014-0440

Higgins JE, Biskner A, Sanford G, 2008. Design, fabrication, and testing of the minotaur IV large fairing. Proceedings of the 49th AIAA/ASME/ASCE/AHS/ASC Structures, Structural Dynamics, and Materials Conference, 16th AIAA/ASME/AHS Adaptive Structures Conference,10th AIAA Non-deterministic Approaches Conference, 9th AIAA Gossamer Spacecraft Forum, 4th AIAA Multidisciplinary Design Optimization Specialists Conference. https://doi.org/10.2514/6.2008-1831

Hong CQ, Han JC, Zhang XH, et al., 2013. Novel nanoporous silica aerogel impregnated highly porous ceramics with low thermal conductivity and enhanced mechanical properties. *Scripta Materialia*, 68(8):599-602. https://doi.org/10.1016/j.scriptamat.2012.12.015

Kosareo DN, Oliver ST, Bednarcyk BA, et al., 2014. Buckling design and analysis of a payload fairing 1/6th cylindrical arc-segment panel. Proceedings of the 55th AIAA/ ASME/ASCE/AHS/ASC Structures, Structural Dynamics, and Materials Conference. https://doi.org/10.2514/6.2014-1053

Li SB, Wang ZG, Huang W, et al., 2016. Effect of the injector configuration for opposing jet on the drag and heat reduction. *Aerospace Science and Technology*, 51:78-86. https://doi.org/10.1016/j.ast.2016.01.014

Liao L, Yan L, Huang W, et al., 2018. Mode transition process in a typical strut-based scramjet combustor based on a parametric study. *Journal of Zhejiang University-SCIENCE A (Applied Physics & Engineering)*, 19(6): 431-451. https://doi.org/10.1631/jzus.A1700617

Liu Z, Liu J, Ding F, et al., 2017. Effect of thermochemical non-equilibrium on the aerodynamics of an osculating-cone waverider under different angles of attack. *Acta Astronautica*, 139:288-295. https://doi.org/10.1016/j.actaastro.2017.07.013

Lockwood MK, Petley DH, Martin JG, et al., 1999. Air-breathing hypersonic vehicle design and analysis methods and interactions. *Progress in Aerospace Sciences*, 35(1): 1-32. https://doi.org/10.1016/S0376-0421(98)00008-6

Lv Z, Xia ZX, Liu B, et al., 2017. Preliminary experimental study on solid-fuel rocket scramjet combustor. *Journal of Zhejiang University-SCIENCE A (Applied Physics & Engineering)*, 18(2):106-112. https://doi.org/10.1631/jzus.A1600489

McClinton CR, Rausch VL, Shaw RJ, et al., 2005. Hyper-X: foundation for future hypersonic launch vehicles. *Acta Astronautica*, 57(2-8):614-622.

https://doi.org/10.1016/j.actaastro.2005.03.061

Morshed MMM, Hansen CH, Zander AC, 2013. Prediction of acoustic loads on a launch vehicle fairing during liftoff. *Journal of Spacecraft and Rockets*, 50(1):159-168. https://doi.org/10.2514/1.A32324

Murman SM, Diosady LT, 2016. Simulation of a hammerhead payload fairing in the transonic regime. Proceedings of the 54th AIAA Aerospace Sciences Meeting. https://doi.org/10.2514/6.2016-1548

Sziroczak D, Smith H, 2016. A review of design issues specific to hypersonic flight vehicles. *Progress in Aerospace Sciences*, 84:1-28. https://doi.org/10.1016/j.paerosci.2016.04.001

Wang L, Zhu GX, Guan CQ, et al., 2016. Experimental investigation of dynamic separation for an inlet cover in Mach 6.0 flow. Proceedings of the 32nd AIAA Aerodynamic Measurement Technology and Ground Testing Conference. https://doi.org/10.2514/6.2016-4111

Yang XX, Zhou Z, Peng K, 2014. Aerodynamic shape design optimization of fairing based on kriging method. *Journal of Solid Rocket Technology*, 37(2):167-171 (in Chinese). https://doi.org/10.7673/j.issn.1006-2793.2014.02.005

Zhang XM, Yang SL, Li P, 2017. Numerical simulations of the inlet cover opening process. *Journal of Solid Rocket Technology*, 40(3):307-312 (in Chinese). https://doi.org/10.7673/j.issn.1006-2793.2017.03.008

Zhao R, Rong JL, Li YJ, et al., 2017. An investigation of fluctuating pressure environment around rocket fairing with different curvetypes. *Acta Armamentarii*, 38(5):1020-1026 (in Chinese). https://doi.org/10.3969/j.issn.1000-1093.2017.05.023

中文概要

题　目：适用于吸气式高速飞行器的蚌式进气道堵盖气动设计及数值模拟研究

目　的：吸气式高速飞行器在助推阶段需要对进气道采取保护措施，而应用传统的圆锥体载荷式整流罩存在体积大、质量重等缺陷。为避免载荷罩的空间雍余，基于激波干扰理论，本文旨在提出一种通用型可实现气动自分离的整流罩设计方法，并探讨设计的两组构型在两个弹道特殊状态点的气动力和气动热特性，以及研究构型的适用性和基本气动性能。

创新点：1. 通过激波干扰理论模型方程，推导出环境变量与构型基本尺寸之间的关系；2. 建立气动设计模型，成功求得助推阶段和整流罩分离状态点的气动特性；3. 新构型减轻了整流罩系统重量，实现了自分离，简化了机械结构系统。

方　法：1. 通过理论推导，得到飞行器头锥长度和进气口尺寸变化对整流罩构型设计的影响；2. 通过数值计算，得到异形整流罩及头锥附近流场分布受设计型面的影响以及产生的适应性气动力。

结　论：1. 整流罩在分离状态可产生负升力，有自动打开的趋势；2. 减小整流罩的设计长度有利于气动减阻和降低峰值热流；3. 整流罩前缘的极限热流约为 13 MW/m^2，在所选复合材料的受热范围内。

关键词：气动外形设计；新型进气道堵盖；气动力分析；气动热评估